An Acad Bras Cienc (2023) 95(Suppl. 3): e20210836 DOI 10.1590/0001-3765202320210836
Anais da Academia Brasileira de Ciências | *Annals of the Brazilian Academy of Sciences*
Printed ISSN 0001-3765 I Online ISSN 1678-2690
www.scielo.br/aabc | www.fb.com/aabcjournal

GEOSCIENCES

Historical line of airglow observations at Comandante Ferraz Brazilian Station: measurements of temperature and studies on gravity waves

JOSÉ VALENTIN BAGESTON, CRISTIANO MAX WRASSE, GABRIEL AUGUSTO GIONGO, EMÍLIA CORREIA, COSME ALEXANDRE O.B. FIGUEIREDO, DELANO GOBBI, HISAO TAKAHASHI, PAULO P. BATISTA & RICARDO A.B. DA COSTA

Abstract: The thermal dynamics of the upper atmosphere, especially in the mesosphere, have been improving our understanding about the effects of climate change, as well as how the dynamics and general circulation in the upper atmosphere are driven by different types of waves, such as the atmospheric gravity waves, planetary waves and atmospheric tides. In order to study the upper atmospheric temperature variability and gravity waves, several research groups have been employing the remote technique of observing the airglow emissions originated in the upper mesosphere and lower thermosphere, besides emissions from the ionosphere. INPE's airglow group started the studies on emissions from the upper atmosphere to investigate temperature and dynamics in the mesosphere, thermosphere/ionosphere at the end of 70's. However, only in 2001 this group sent the first airglow experiment to the Brazilian Antarctic Station Comandante Ferraz (EACF) to measure the OH (8-3) emission and temperature. From that year to 2014, several other experiments were carried out at EACF, not only to measure the temperature and airglow intensities, but also to observe gravity waves, winds and other related phenomena. This paper presents airglow experiments at EACF from 2001 to the present, including illustrations, examples of already published results, and unpublished data.

Key words: Mesosphere, Antarctica, Mesospheric Temperature, Atmospheric Gravity Waves, Atmospheric Coupling.

INTRODUCTION

The upper atmosphere, including the upper mesosphere, lower thermosphere and ionosphere (MLTI) is controlled by the Sun energy. In the MLTI several type of waves, thermal changes (mesospheric inversion layers) and winds (or wind shears) affect that region, and from the lower atmosphere the gravity waves that reach the upper mesosphere also plays an important role in the local dynamics. The determination of temperature in the upper mesosphere region (~85-90 km) is very important because, apart from the knowledge of the thermal structure of the atmosphere, this variable can also be used for monitoring possible global climatic changes (Roble & Dickison 1989, Rind et al. 1990, Golitsyn et al. 1996). The process of estimating the temperature in the mesopause region (~87 km) from the hydroxyl radical (OH) emissions in several bands is already well established since the first indications of the use of these emissions as a tracer for the atmospheric temperature (Meinel 1950). Since then, several works have used this technique to determine the temperature in the mesosphere, such as Takahashi et al. (1974), Buriti et al. (2000), Phillips et al. (2004), Wrasse et al. (2004), Bageston et al. (2007), among many others.

The mesospheric dynamics is dominated by atmospheric gravity waves (GWs) that present periods ranging from about 5 minutes to a few hours, and horizontal scale from meters to hundreds of kilometers (gravity waves), whereas global scale waves, or planetary waves have very large horizontal wavelength structures (tens of hundreds of km) and periods of 8, 12 or 24 hours (atmospheric tides) or days (4, 6, etc.). By using the airglow technique as a tracer of the atmospheric dynamics, we can access through night-sky images only gravity waves, but if there is available long (and continuous) time series of temperature and airglow intensity, it is also possible to study planetary waves and tides. However, if temperature or airglow intensity data is available only for one station, it is not possible to access information on the spatial structures of these waves. One important advantage of the usage of airglow images to characterize gravity waves is that a full set of information can be obtained, such as horizontal wavelength, period, velocity and propagation direction. It is also possible to visualize wave-wave interaction or wave breaking locally in the upper mesosphere when the interval between sequential images is sufficient short (e.g., less than 30 s for a single OH filter).

The Antarctic Peninsula region, including the Drake Passage, shows an intense gravity wave activity and this region is known as “hot spot” of gravity waves from the stratosphere to the upper mesosphere and lower thermosphere, and the most studies based on satellite and reanalysis data have been done for the middle atmosphere (e.g.: Jiang et al. 2006, de la Torre et al. 2012, Hindley et al. 2015, Hoffmann et al. 2016), but this large gravity wave activity also extends to the upper mesosphere and lower thermosphere. The main reason attributed to this large wave activity is the very intense horizontal winds over that region; the large amplitude thermal gradients; the location of cold fronts formation; the occurrence of mountain peaks near the Antarctica Peninsula and to the north, there is the presence of the southern extended Andes mountains. In the lower stratosphere gravity waves have been found to produce temperature decreases at the ascending phase of the wave that drop local temperatures below critical levels favorable for the creation of nitric acid trihydrate (NAT) or ice, leading to the formation of mountain wave-induced polar stratospheric clouds (PSCs) (Jiang et al., 2006 and references therein). In the Mesosphere and Lower Thermosphere (MLT) region despite of the known large gravity wave activity as revealed by all-sky airglow imagers, the character of GW forcing of the MLT remains largely unknown, however, as systematic global measurements able to quantify all the relevant scales are not yet possible. While the major sources are known qualitatively, the contributions of GWs filtering, interactions, spectral evolution, source intermittency, and waves localization are still poorly understood (Fritts et al. 2014).

It is very important to study the gravity waves and their impact in the atmosphere since forcing due to these waves can cause, besides impact in the local temperature and/or winds/turbulence, reversals of the zonal mean jets and drive a mean meridional transport circulation in the MLT region, which leads to latitudinal temperature gradient opposite to that expected in the absence of wave forcing (Fritts & Alexander 2003). Recently, using EACF station airglow imaging, two different kinds of studies were conducted: the first one focused on mesospheric fronts (Giongo et al. 2018), whereas the second one is an investigation about wave filtering of the mean winds, while it propagates from the lower to the upper atmosphere by using the blocking diagrams (Giongo et al. 2020).

Nowadays, our society is widely dependent on meteorological forecasting and technological devices, such as GPS and modern vehicles. In this context, a complete understand of our atmosphere is absolutely necessary, realizing how the parameterizations of waves (including GWs) can improve meteorological predictions by one side, and on the other side, how gravity waves can induce ionospheric density fluctuations that can interfere in the electromagnetic waves propagation, affecting GPS users, power grids, high frequency communication, etc. This paper revises the observational techniques used at EACF since the years 2000's, and shows some sets of unpublished data on temperature and gravity waves.

MATERIALS AND METHODS

The MLT instruments already operated at EACF (62.1°S, 58.4°W) are passive optical instrumentation (photometers, imaging spectrometer, all-sky camera and photographic camera) and an active radio wave instrument named meteor radar, which includes transmitting and receiving antennas, and electronic modules.

Since we have several instruments in operation at EACF to observe the mesosphere and lower thermosphere, then it was possible to produce essential data that allowed the production of important scientific results over years. Table I presents both the data availability of each instrument from 2001 up to 2023, as well as the data quality of each instrument in the same period. The discontinuity in the data acquisition occurred due to the fire at the EACF in 2012, since it was not possible to operate and maintain the scientific instruments continuously while the station was being rebuilt up to 2019.

The optical instruments, according to their time of installation and operation, are described just below.

Zenithal Photometers - FotAntar-1 and -2 (years 2001-2004)

The first instrument installed at EACF was a portable photometer named "FotAntar-1", operated at EACF between 2001 and 2003. It is a device designed to measure the emission lines of the P branch of OH (8-3) airglow band in order

Table I. Instrumentation operated at EACF from 2001 to 2023.

Instrument	Period	Data Quality
Tilting filter photometers (FotAntar-1 and -2)	2001-2004	Good
Temperature Imaging - CCD (FotAntar-3)	2005-2010	Good (2005-2007); Reasonable (2008-2010);
Temperature Imaging - CCD (FotAntar-4)	2011	Good
Low-cost all-sky imager (single filter – OH)	2007; 2010-2011	Good
High-performance all-sky imager (filter wheel – 3 filters: OH, OI 557.7nm and OI 630.0nm)	2014-2017; 2022-2023	Discontinuous (2014; 2018-2021); Good (2015-2017; 2022 up to now)
Photographic camera for Noctilucent Clouds (NLCs)	2014-up to now	Discontinuous (2015-2019); Good (2020 up to now)
Meteor Radar	2010-2012 (up to Feb.), 2019-up to now	Good (2011; 2022 – up to now); Reasonable (2010, 2020 - 2021);

to determine the temperature in the mesopause region. This photometer has a tilting-filter, an optical system with objective lens and a photomultiplier (PMT) tube as detector. The total aperture of the FotAntar-1 is 2.5°, and due to the field stop diaphragm and the associated optical configuration, the photometer yields a field of view of 2.5° × 8° which corresponds to an area of about 4 km × 12 km (48 km^2) at the OH emission layer (around 87 km of altitude) (Wrasse 2000, Wrasse et al. 2004). Also, there are electronic parts that control the high voltage (HV) in the PMT, a pre-amplifier (PA) and a discriminator of frequency, as well as a step motor M1 for filter tilting, and M2 for calibration disk rotating (Wrasse et al. 2004). Figure 1 shows a picture of FotAntar-1 (bottom) and the first dome installed behind the hills at Punta Plaza shelter nearby EACF, in order to avoid light contamination from the main station and vicinities modules.

The schematic optics diagram of FotAntar-1 and more information on the calibration process performed in this instrument can be found in Wrasse (2000) and Wrasse et al. (2004).

In order to obtain the temperature and OH (8-3) band intensity, the photometer measures the spectrum of the P branch of OH (8-3), and by tilting the filter it can scan the wavelengths from 732 to 742 nm, solving the spectral lines $P_1(3)$ at 734 nm, $P_1(4)$ at 736.9 nm and $P_1(5)$ at 740.2 nm. The background position was chosen to be at 738.2 nm (Wrasse, 2000), and the time resolution of the temperature and intensities measurements was about 3.5 minutes. The intensity ratio between $P_1(5)$ and $P_1(3)$ was used to calculate the rotational temperature (associated to the rotational emission lines), or just temperature / kinetic temperature, which was obtained with a systematic error, due to the filter transmittance and PMT sensitivity, of ±2.5 K and an error in the OH (8-3) band intensity less than ± 6% (Wrasse 2000). It is important to

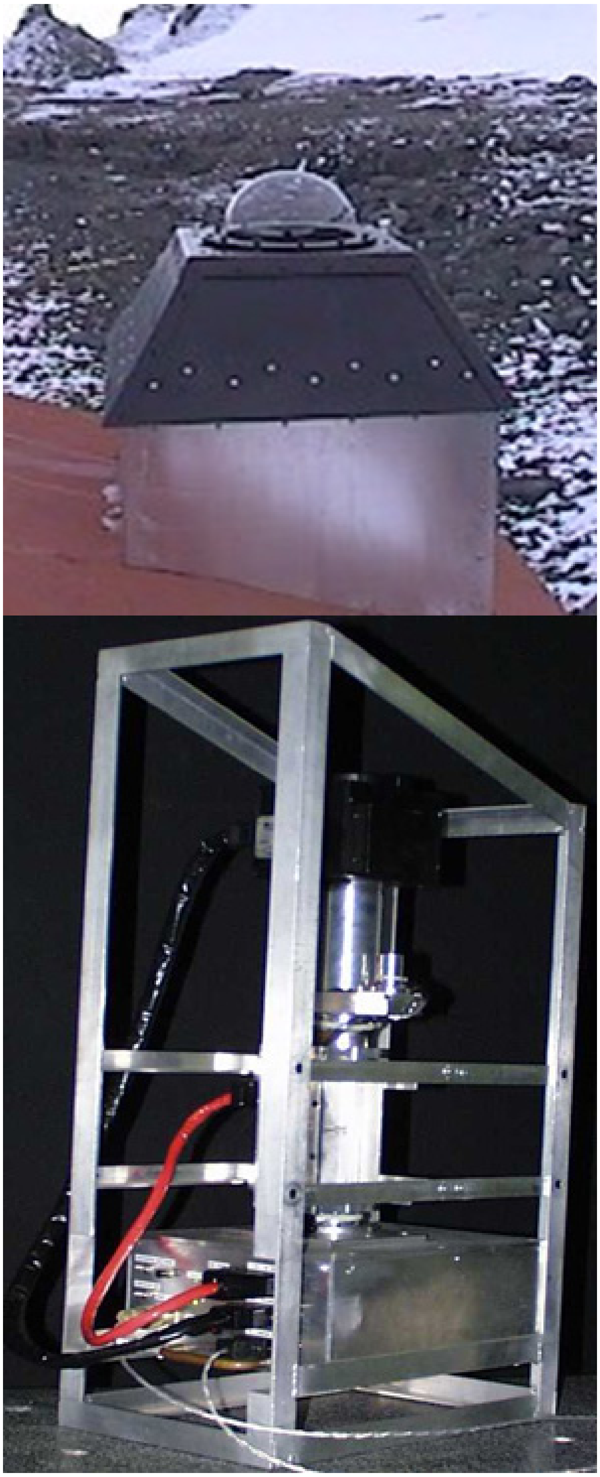

Figure 1. Glass dome at the roof of Punta Plaza shelter (top) used to house the FotAntar-1 instrument (bottom).

note that all the assembling and instrument calibration were conduct at the Airglow INPE's Group in São José dos Campos, SP.

The FotAntar-2 photometer was adapted from the multichannel 2 photometer (MULTI2), but with one filter for the OH (6-2) emission, operated primarily at LUME observatory in Cachoeira Paulista, SP, and later on operated at EACF for just one year (2004). In 2005 it was used a new generation of sensor (in the same spectral band), which used a CCD as detector instead of a PMT (see details in the next session). The photometer FotAntar-2 is more complex, larger and heavier than FotAntar-1, but had the benefit of having an efficient cooling system for the PMT tube and the time resolution was higher than the previous one (~ 2 minutes), whereas the total field of view is similar to the previous instrument (2°). In a similar way to the FotAntar-1, the FotAntar-2 system was composed by three basic units: an optical system, an acquisition interface, and control units. In the OH (6-2) band of the hydroxyl, P is the observed branch in the wavelength interval between ~ 836 and 848 nm, solving the main rotational lines: $P_1(2)$ at 839.9 nm, $P_1(3)$ at 843.0 nm and $P_1(4)$ at 846.5 nm, and additionally the BG position at 843.9 nm. The methodology to obtain the rotational temperature for the FotAntar-2 photometer is the same as the FotAntar-1, except that in this case the temperature is obtained by the ratio between the lines $P_1(4)$ and $P_1(2)$.

Imaging Spectrometers "FotAntar-3 and -4" (years 2005 – 2011)

During the years of 2003 and 2004, a new generation of photometers that used a CCD camera as an efficient photon detector were developed. With the addition of an adequate filter and an optical system, it would be able to resolve the spectral rotational lines in a given airglow band. This new system was named 'temperature imaging spectrometer' since the output of data was an image forming several spectral lines (concentric rings, similar to the Newton's rings) due to the diffraction of the light in the filter (reaching it at distinct angles regarding the zenith) and the optical configuration.

The first new system, named FotAntar-3, was operated (after laboratory calibrations) at INPE's airglow observatory in the municipality of Cachoeira Paulista, SP, from March to May, 2005. The objective of this short campaign was to obtain the first field data, testing distinct methods of image processing to obtain the temperature and airglow band intensity, and finally compare the temperature results with the MSISE-90 atmospheric model and with other co-located photometer (MULTI-2) to validate these first results before shipping the FotAntar-3 to Antarctica. The details of the calibration, error analysis and comparisons with the MSISE-90 model and the zenith tilting-filter photometer can be found in Bageston (2006), and Bageston et al. (2007). FotAntar-3 imaging spectrometer operated at EACF from mid-2005 up to 2010, and in 2011 it was replaced by another similar CCD imager because since 2007 presented problems in the collected images (with readout problem in the CCD, generating horizontal noise lines). The system has a field of view of 22°, given an imaged area at the OH layer with about 70 km of diameter. The spectrum range imaged by this system was from ~836.2 nm to 847.0 nm. The methodology of estimating the temperature based on the images is well detailed in Bageston (2006) and Bageston et al. (2007), but the main idea is following a sequence of image process, i.e., dark current (or dark noise) subtraction (by acquiring a "dark" image, with the shutter closed between a certain time interval, e.g., 30 min). The process is done by performing the following steps: 'sky image' minus 'dark image'; find the center of the rings; integrate the image from the center to the border (generating a profile); detrend the profile through a linear fit, and subtract the BG. The detrending of the original profile is based on the photon count at the background level (BG) position, and also based on the BG count calculated for the $P_1(4)$ and $P_1(2)$ peak positions.

Figure 2 shows the optical facilities where the photometers and CCD spectral imager were installed. In the bigger dome on the left, first were installed the FotAntar-1 and -2, which were replaced by an all-sky airglow imager, and in the smaller dome it were operated the FotAntar-3 and FotAntar-4 systems, which were composed by a CCD camera, objective lens, filter, aperture window, step motor and Fresnel lens. The FotAntar-4 imaging spectrometer is shown on the bottom-right side of Figure 2. We need to point out that the photo was taken at the INPE's airglow laboratory. It should also be noted that a protection (house) and a shutter (not shown in Figure 2) were installed in the optic system for protection even though the instrument would be operated inside a shelter, this certainly would give extra protection for the CCD while it was exposed to sunlight during the daytime (the airglow phenomena can be observed only in the nighttime).

Figure 3 shows an example of image acquired by the FotAntar-3 (after subtracted the dark noise) where it was drawn two black circles to identify the region between two spectral lines as the background region (BG position), and the airglow spectral lines used to estimate the temperature are also identified on the image. On the right side of Figure 3 are presented the integrated profiles plotted as a function of the respective wavelengths, and also the spectral lines and BG are identified over its respective position.

The temperature (in Kelvin, K) is obtained by using the lines $P_1(4)$ and $P_1(2)$, while the band intensity (in Rayleigh, R) is calculated based on the estimated temperature and in one relative intensity of any of the measured spectral lines in the band. The exposure time of each image is 1 minute, but the average time resolution of the temperature (and intensity) is about 1.5 minutes since there is a delay due to the dark

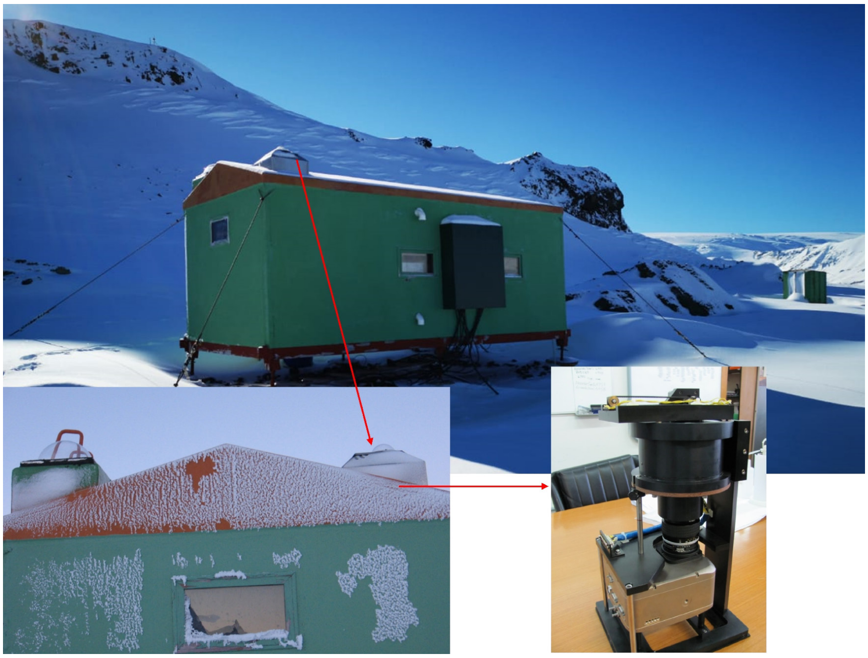

Figure 2. Punta Plaza module with two domes, and the FotAntar-4 (similar to the FotAntar-3) on the bottom-right side.

image acquisition (at every 30 minutes) and the recording time for each image. The systematic errors in the temperature and OH (6-2) intensity are about ±1 K and 1%, respectively.

The FotAntar-3 was replaced by the FotAntar-4 in 2011, and operated just for one winter because of the fire accident at EACF in February of 2012. The FotAntar-4 was very similar to the FotAntar-3 system, except that the latter communicated with the computer via a USB connection instead of a VGA-type of data transference, and the calibration is quite different since both filter and CCD present intrinsic characteristics of bandwidth (transmittance) and sensitivity, respectively, which are distinct from one system to another. However, data collected with the FotAntar-4 were not analyzed yet, and the data from FotAntar-3 between 2008 and 2010 were not used up to now due to problems in the images.

All-Sky Airglow Cameras: single filter (2007; 2010-11) and Multifilter (2015-2017)

All-sky imagers (with CCD detectors in the body of the cameras) are optical devices designed to measure the nightglow (airglow emissions during nighttime) in the mesosphere (80-100 km altitude) and thermosphere/ionosphere (200-300 km altitude). The first all-sky imager installed at EACF was in March 2007 to conduct a full winter campaign during that year. The used imager during the 2007 campaign (operated until October, 2007) was a low-cost equipment with the following characteristics: a 180° fisheye lens, a 2-inch interference filter wide for the hydroxyl emission bands (715–930 nm, with a notch at 865.5 nm to suppress the O_2 (0-1) emission), and a CCD camera (model SBIG STL-1001E model) coupled to a telecentric lens system. More details about this instrument can be found in Bageston et al. (2009). Later on, in 2010, the same system was reinstalled at EACF and operated during the austral winter of 2010 and 2011. In 2014, a modern all-sky imager was installed at Punta Plaza shelter, but during May of that year the electrical cables and the power transform nearby Punta Plaza had problems, and it was not possible to obtain any data in the winter of 2014. After fixing those problems in the summer of 2015, the new system was back to operation

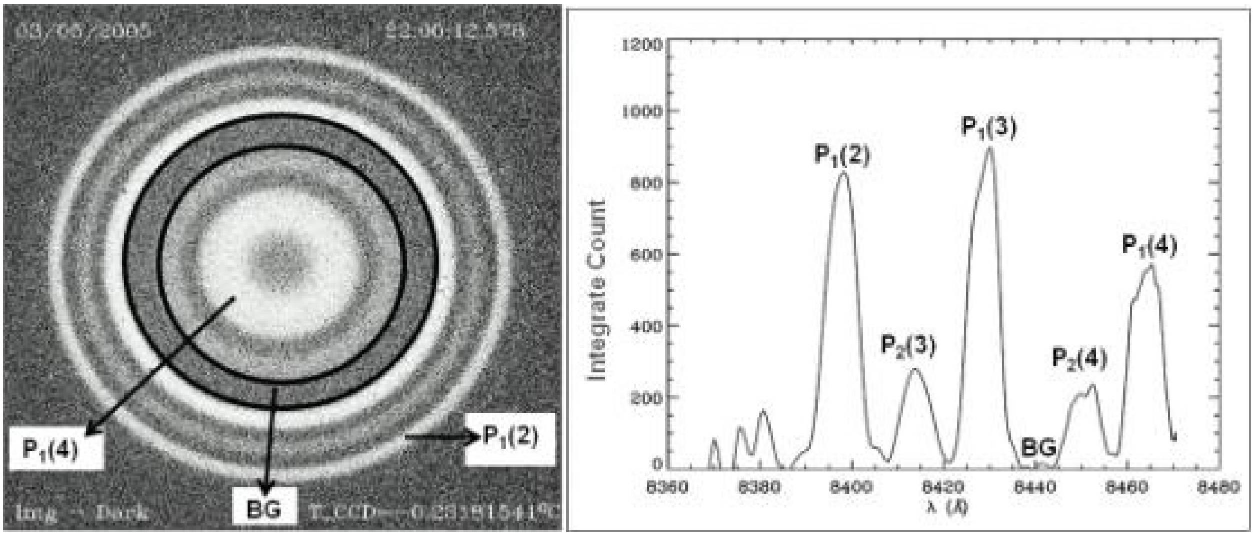

Figure 3. Example of image obtained by the FotAntar-3 imaging spectrometer (left) and the representation of the same image as an integrated (from the center) profile in wavelength scale (central ring is the P_1(4) while P_1(2) is the last ring in the image). Source: Adapted from Bageston et al. (2007).

up to the end of 2017, but unfortunately, in 2018, the all-sky imager presented problems and did not operate anymore, until it was removed from Antarctica in February 2019. This modern all-sky imager has a fisheye lens with a 180 degrees field of view, 3-inch narrowband interference filters to measure the near-infrared hydroxyl (~715–930 nm), OI 557.7 nm and OI 630.0 nm airglow emissions, and a telecentric lens system to project the image onto a 1024 x 1024 pixels CCD camera. More details on this instrument can find at the Keo Scientific site (http://keoscientific.com/space-science.php).

The all-sky imagers at the observation site and examples of images are shown in Figure 4, where the red arrows indicate the same bigger dome that was used to host both all-sky cameras during six years of good data (2007, 2010-2011, 2015-2017). A new high-performance all-sky imager, similar to the one operated between 2015 and 2017, was installed at EACF in January 2022 and it is currently in operation, obtaining good data from Feb. 2022 up to the current year (2023). We hope that this instrument can continue in operation for a long time.

The methodology to analyze the images obtained by an all-sky imager includes at first a pre-processing (Garcia et al. 1997, Medeiros et al. 2003, Wrasse et al. 2007) as follows: first, the top images are rotated to the geographic North; second, the starfield is subtracted from each image (Maekawa 2000); third, the original images are unwrapped to a new coordinate system, as the projection of the night sky on the CCD camera is distorted due to the shape of the fisheye lens.

After pre-processing the images, we apply digital filters to highlight the geophysical

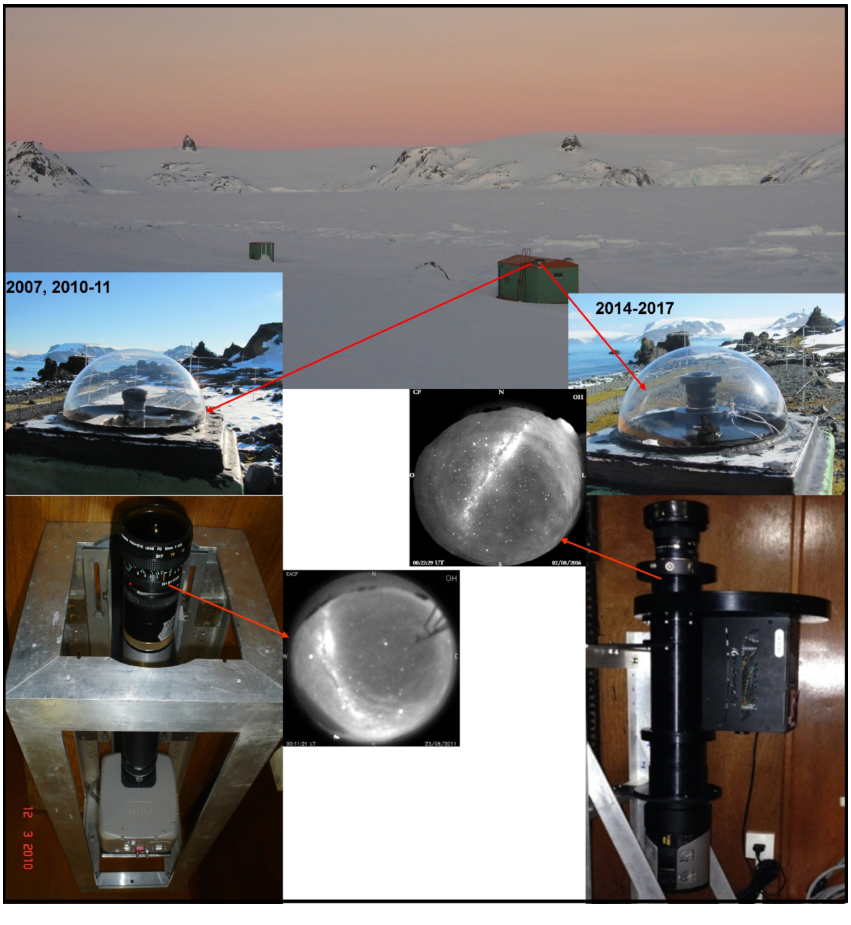

Figure 4. Punta Plaza facilities with the frozen sea (top), the all-sky airglow imagers, and their respective examples of images on the left (low-cost imager) and right (high-performance imager).

phenomena and properly remove the frequencies that would interfere in the spectral analysis (e.g., Bageston et al. 2011a, Wrasse et al. 2007). After these processes, in order to obtain the gravity waves parameters (observed phase speed, horizontal wavelength, and observed period) it is applied a cross-spectrum 2-D Fast Fourier Transform (FFT) to a sequence of images (Wrasse et al. 2007).

RESULTS

This session presents the main results from EACF, concerning both mesospheric temperatures and gravity waves.

Temperatures from Zenithal Photometers and Imaging Spectrometer

Temperature and airglow band intensities normally are changeable in time, responding to atmospheric typical oscillations and also presenting the natural daily and seasonal variations.

Figure 5 summarizes the daily temperature (nighttime average) for the FotAntar-1 and -2,

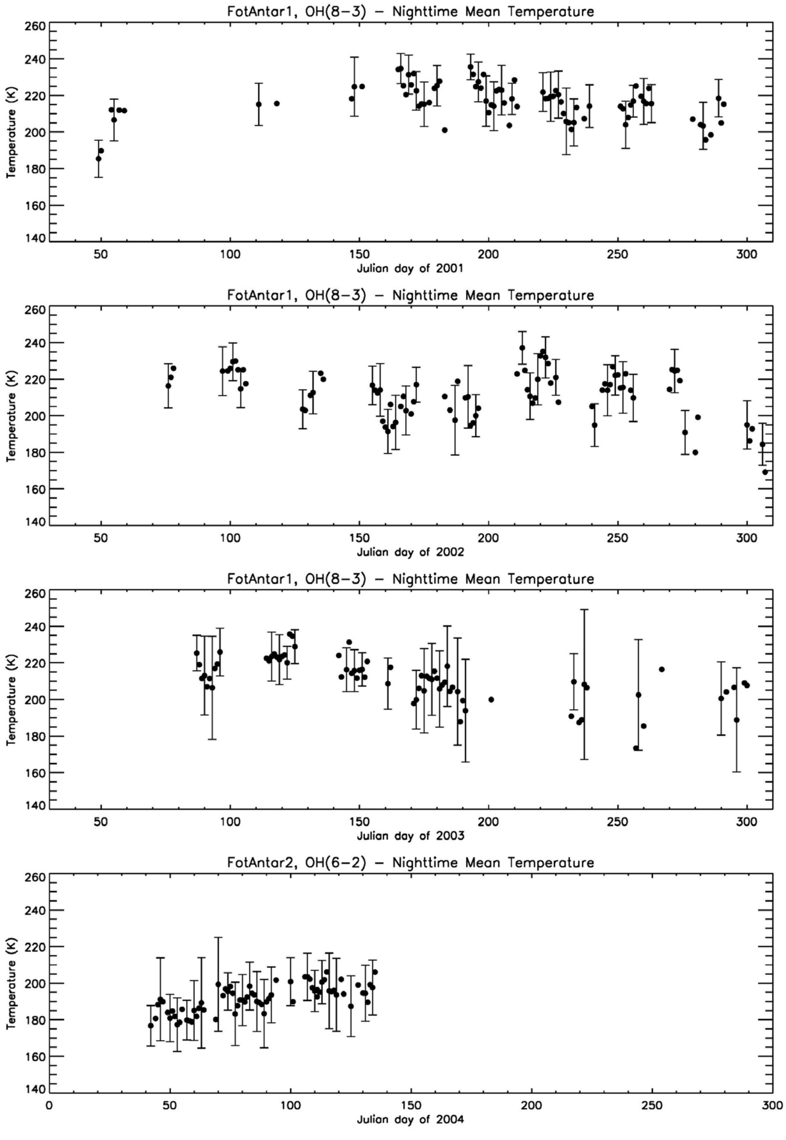

Figure 5. Rotational temperatures based on the OH(8-3) emission (FotAntar-1), from the top to the third panel, and based on the OH(6-2) emission (FotAntar-2) on the bottom.

from 2001 to 2004. The error bars represent the standard deviation of the nocturnal average. It is possible to see clearly that temperatures measured based on the band OH(8-3) are quite higher than the values obtained by the OH(6-2) band emission. Differences in the temperatures can be attributed to the use of distinct Einstein coefficients (Wrasse et al. 2004), but in this case, we used the same set of coefficients given by Langhoff et al. (1986). Here the average temperatures from 2001 to 2003 are between 210 and 215 K, and in 2004 the mean temperature for the available data is ~192±7 K. The difference of about 22 K is quite large but could be explained by the emission band itself since different spectra respond in distinct ways to the reemission energy, and consequently the associated temperature can be slightly distinct. Another explanation is from the instrumental point of view because the two photometers are distinct in technical terms and could be subject to distinct local environment (temperature/humidity) conditions, and as it knows, the internal temperature at the shelter can interfere in the observed spectrum, and consequently in the final calculated temperature for the mesosphere (indirect estimation), and a more adequate and systematic calibration in the instruments to correct the above interferences could minimize these large differences in the temperatures. Temperatures from FotAntar-2 (2004) and FotAntar-3 (2005-2007) are shown in Figure 6. As mentioned before, for FotAntar-1 and -2, and also in the case of FotAntar-3, the temperature was calculated based on the Langhoff coefficients and the observed airglow band in both FotAntar-2 and -3 is the OH (6-2). Here we need to note that, despite the fact that the instruments observe the same band, there are technical differences between these two instruments, i.e., the new FotAntar-3 uses a CCD as detector, instead of a PMT used by the former FotAntar-2. The type of collected data is also very distinct: FotAntar-3 generate images, while the previous photometer generated a time series of numerical data.

For 2005, the average temperature, as observed by FotAntar-3 was about 185 K (days 150 to 290), and this value is quite similar (just 7 K of difference) to the mean of FotAntar-2, as observed in 2004, even knowing that the time intervals are not overlapped. In 2006, only about two months of observations were possible to get, and the mean temperature was almost the same as observed in the previous year. During 2007, it was possible to obtain a large interval of good data. The mean temperature for 2007, as calculated from FotAntar-3, was the same as in the previous two years, always in the interval between 160 K and 200 K, considering the standard deviations.

In terms of seasonal variations, the above results do not allow us to discuss in a proper manner, since not all the observed years had full data throughout the year, but typically we can identify a lower (minimum) temperature near the end of the summer (days 40 to 60) and at the end of the spring (days 260 to 300), while in the winter the temperature tend to be higher (crossing the limit of 230 K, as observed by FotAntar-1, and around 220 K – considering the standard deviation – as observed by FotAntar-2 and -3). In 2007, when it was possible to observe the longest time series of the mesospheric temperature in a single year, we can clearly see that also occurred an unexpected minimum temperature during the winter (days 180 to 200), with a maximum before (around day 140) and after (around day 215) the minimum, while it was not seen this behavior in 2001-2003 and 2005. We already confirmed that this minimum temperature was also observed by the TIMED/SABER satellite around day 190. This 'oscillating' behavior needs to be better investigated,

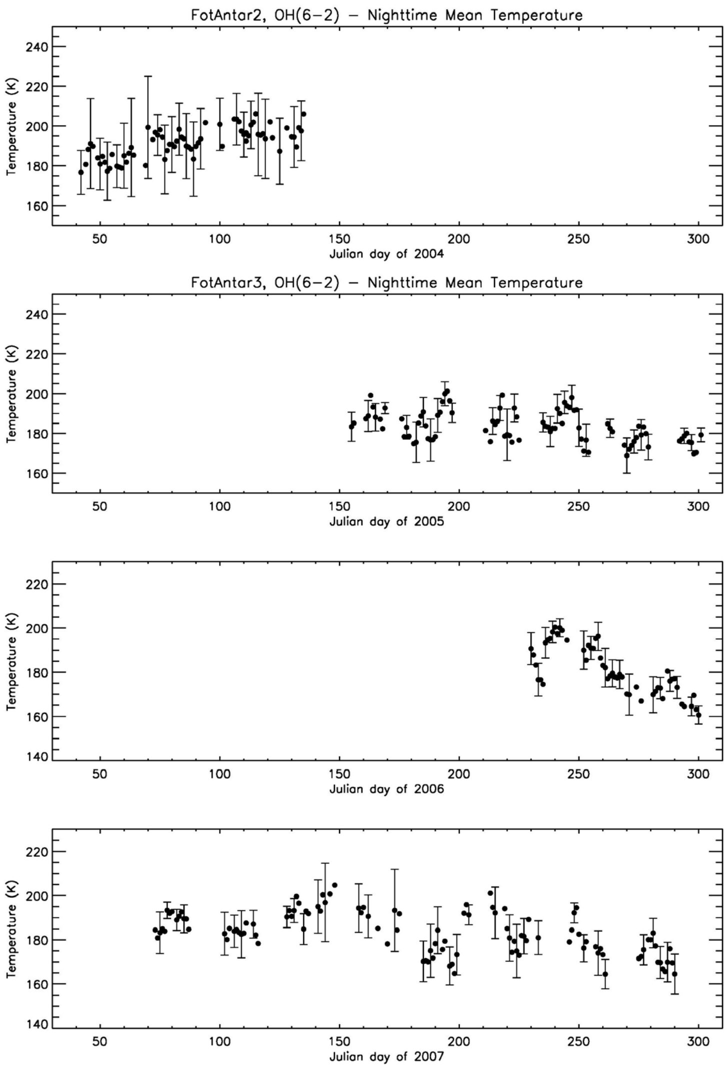

Figure 6. **Rotational temperatures based on the OH(6-2), as observed by FotAntar-2 (top: 2004) and FotAntar-3 (second to third panel: 2005-2007).**

but probably it can be attributed to the local dynamic associated with planetary waves.

On the other hand, year-to-year temperature variability between 2001 and 2004 are comparable with the MSIS-90 model. In terms of averages, the model shows smaller temperatures than FotAntar-1, and very similar absolute values to the FotAntar-2, as can be clearly seen in Figure 7. By comparing the nighttime variability of the temperature of the FotAntar-3 and MSIS-90 model, at several days, the time series are very similar (not shown here) and it can be checked in Bageston et al. (2007).

Figure 7 shows clearly that both ground-based instruments and models present great similar variability, but the temperature from the Czerny-Turner spectrometer seems to be smaller than the FotAntar-1, especially for 2001. For 2002, the data sets are in very good agreement. However, some differences in the observed nighttime temperature could be noted and may be due to the geographical location of both observation sites. The distance between Ferraz (62.1°S, 58.4°W) and Davis (68.6°S, 78°W) station is around 5,000 km, which means that the atmospheric dynamics and chemistry could change the mesospheric temperature over each station in a different way. The Antarctica Peninsula region, where is located the Ferraz station, is known as a hot spot of gravity waves

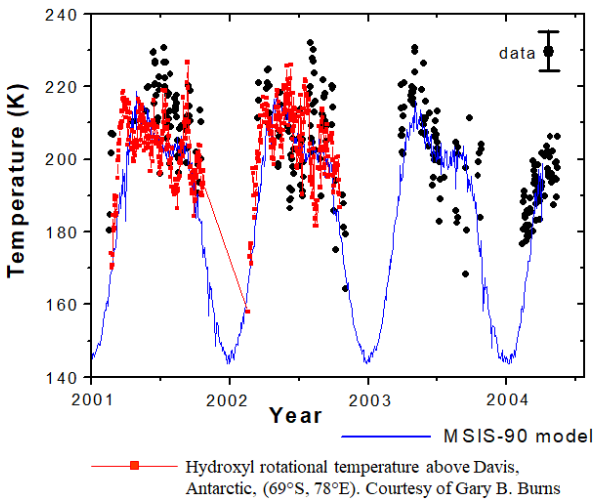

Figure 7. Mean rotational temperatures (black) based on the OH (8-3) (FotAntar-1) and OH(6-2) (FotAntar-2) for comparisons with the MSIS-90 (blue) and Czerny-Turner grating spectrometer (red) that measures the OH(6-2) airglow.

mainly due to the very intense winds over the Drake Passage and the presence of high mountains in southern Chile and Argentina. Also, planetary waves in this region could change the neutral temperature causing a day-by-day variability and consequently changing the temperature monthly average. Another important fact in the temperature differences could be the lack of annual calibration and the ideal environment as mentioned earlier. Therefore, an extra calibration in the photometers operated at Ferraz station could mitigate the temperature discrepancies between the distinct instruments. It is also possible to see in Figure 7 that the overall average temperature observed by the MSIS model is much lower than the airglow photometers data, and this is because the model includes the full period of the years (in the summer the temperature is lower in the mesosphere than in the winter), and the ground-based instruments observe mainly in the winter (higher temperatures compared to the summer). When we look at the winter-time, the mean temperature of both photometers and model are very similar and in the years 2003 and 2004 the average temperatures of FotAntar-1 and 2 match very well with the MSIS-90 model.

Recently, French et al. (2020) presented a long time series (24 years) of temperature over Davis station, Antarctica. Their observations and trend analysis are compared with the AURA/MLS satellite. Our perspective is to perform a similar analysis as French et al. (2020), but using both SABER and MLS instruments on board of TIMED and AURA satellite, respectively.

Gravity Waves from All-Sky Imagers

Atmospheric gravity waves were observed at EACF in the following years: 2007, 2010-2011, 2015-2017. During the 2007 campaign, many types of gravity waves were identified, including “bands”, mostly, a little of ripples (less than 20), and just a few events (~ 4) of mesospheric fronts or bores. Bageston et al. (2009) presented the main types of observed waves and characterized all the ~ 240 gravity wave events identified during the campaign. Specific frontal types of gravity waves identified in 2007 were reported by Bageston et al. (2011a, b), which were classified, respectively, as mesospheric wall and mesospheric front (or bore), and both were found to be propagating in mesospheric ducts.

The observations of 2010-2011 were reported partially (observed parameters only for 2010) by Bageston et al (2012). This short report showed that the observed characteristics of the gravity waves were similar to the ones obtained in the observations of 2007. The number of observed events in these years were much smaller than in 2007 (2010: 74 events; 2010: 123 events).

The full set of data for 2010 and 2011 indicated the presence of 223 gravity wave events (74 in 2010 and 149 in 2011). Figure 8 presents a histogram of the observed parameters for these two years. Typically, the wave parameters are quite similar to the previous observation, showing that most

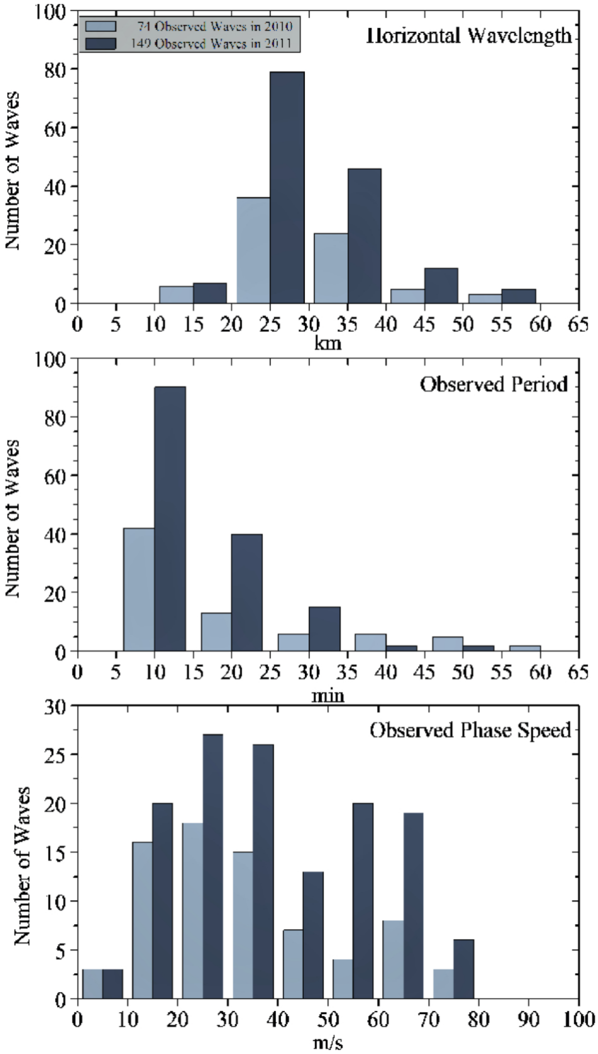

Figure 8. Observed parameters of gravity waves identified at EACF during 2010-2011.

waves have horizontal wavelengths smaller than 40 km, periods typically between 5 and 10 min, and observed phase speed in a wide range, mainly from 10 to 70 m/s.

In 2010, we could not identify any mesospheric front, but in 2011 some interesting frontal waves were observed, as it can be seen in the examples showed in Figure 9, that contains a sequence of images of the event of Aug., 22-23 (first row) and Aug. 28-29. The red arrows denote the direction of the wave fronts propagation, and a small white arrow on the last image indicates another gravity wave propagating to the southwest (probably generated locally caused by the dynamic instability generated by the frontal wave dissipation). Over the first image of each sequence is identified the wave observed parameters, and it is important to note that in both cases the waves propagate with a relatively high velocity (~ 89 and 60 m/s, respectively). The high phase speed of the wave and the well-defined leading wave front that extends from one side to the other part of the image (even more than 400 km in extension) are typical characteristics of mesospheric wave fronts.

Giongo et al. (2018) reported and characterized four frontal types of waves, including the two events showed previously in Figure 9. In that work (Giongo et al. 2018), the authors also investigated the potential wave sources for the observed events, and two of them could be associated with lower troposphere instabilities, whereas other two cases could not be linked to tropospheric sources. Potentially, these latter events would be generated by local wind shear in the mesosphere, or alternatively could be attributed to secondary wave sources in the upper stratosphere or mesosphere.

Giongo et al. (2020) presented the characteristics of the waves observed during 2017, and conducted a study on the wave filtering process due to winds along the path from the lower to the higher atmosphere by using observed winds obtained by the meteor radar located at King Sejong Station - KSS(62.1°S, 58.7°W), and the ERA-5 reanalysis from ECMWF (European Centre for Medium-Range Weather Forecasts) to complement the data from the ground up to 80 km height. Besides the full-year analysis, Giongo also investigated the wave filtering by using a short time scale (nighttime period) to construct the blocking diagram and investigate eight (8) events of small-scale waves and one (1) medium-scale wave, also applying

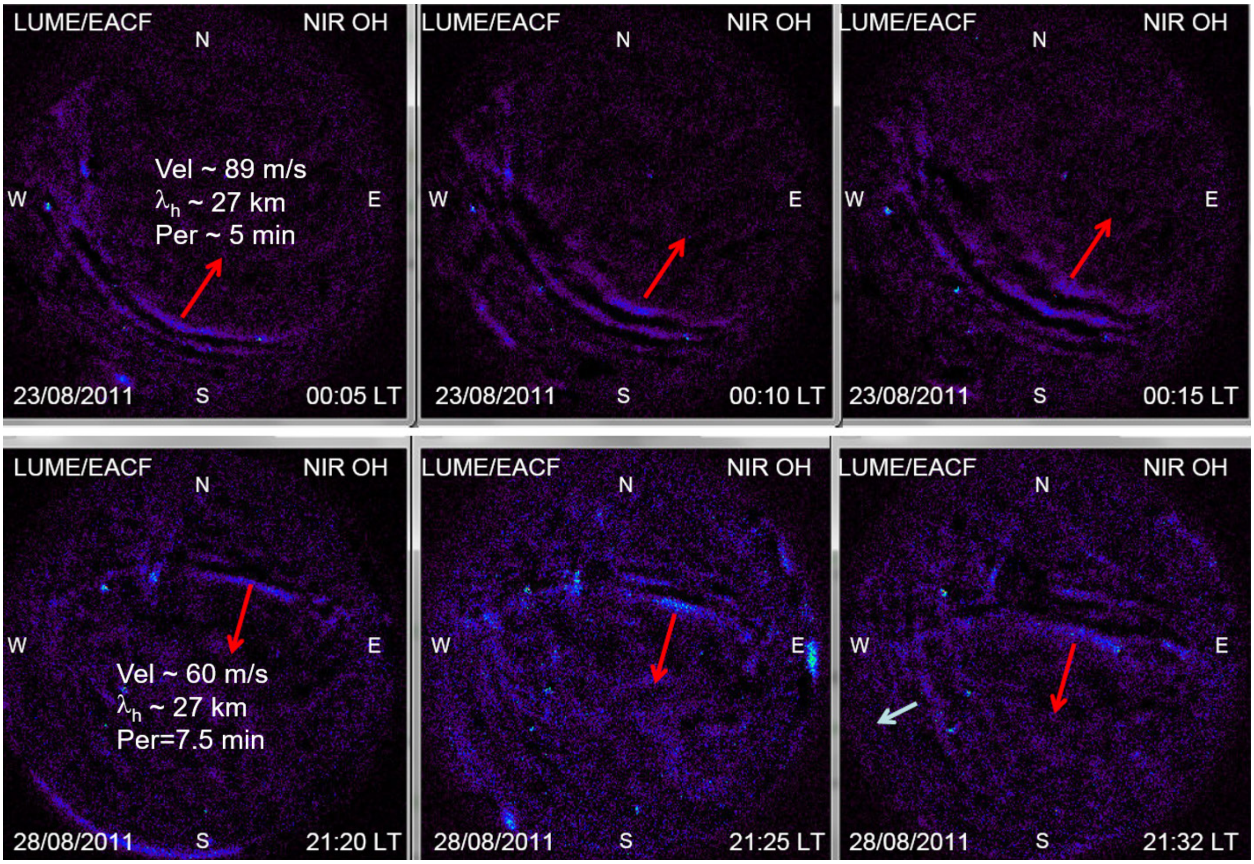

Figure 9. Examples of mesospheric fronts observed at EACF during the nights of August 22-23 (top) and 28-29 (bottom) of 2011.

the ray-tracing technique to these events in order to identify their potential sources.

Besides these important results obtained at EACF, a recent work reported large gravity wave activity nearby Ferraz (KSS station) by using meteor radar and all-sky imager (Song et al., 2021) and in the Antarctica pole unexpected occurrence of mesospheric wave fronts over the South Pole was also reported by Pautet et al., (2018). Frontal wave events were considered rare for Antarctic latitudes (e.g., Nielsen et al. 2006 and Bageston et al. 2011a), but recent new results (e.g., Giongo et al. 2018 and Pautet et al. 2018) indicate that such events are more commons than previously thought, especially for high latitudes near the south pole. On the other hand, the source of these wave events is a puzzle that only can be solved by using complementary data (e.g., Mehta et al. 2017, Rourke et al. 2017 Hozumi et al. 2018 and Giongo et al. 2020). A very recent work (Kogure et al. 2023) presents gravity waves observed over Syowa and Davis stations simultaneously during the main winter of 2016, presenting and discussing the characteristics of phase velocity spectra and power spectra density.

Other types of gravity waves are the medium and large-scale gravity waves with scales larger than about 70 km, up to about 500 km in its horizontal wavelength, and such events can be identified and characterized by using a technique called keogram (see, for example, Paulino et al. 2011 and Essien et al. 2018). This technique is based on the original all-sky airglow images, using unwarped images, projected in geographic coordinates (linearized), without stars and digitally filtered to cut-off the lower frequencies (the higher frequencies are filtered when the star-field is removed). Figure 10 shows an example of this kind of data for a full night keogram on the left, labeled as (A), and a region of the selected area where the wave is analyzed on the right side, labeled as (B). The red boxes on the left identifies the regions of analysis (using Fast Fourier analysis in this case), and the arrows indicates the respective region in the right-side picture. The red dotted lines on the middle graphic of Figure 10 (B) indicates the 95% confidence level for the maximum spectral energy in the Fourier spectrum, and in the lower graphic is the phase difference associated with the Fourier power spectrum. The horizontal wavelength of this event is about 380 km, with an observed period of ~50 minutes and horizontal phase speed of about 127 m/s. This wave is classified as a medium-scale wave, and such kind of wave can carry a large amount of energy and momentum to the upper atmosphere. The medium and largescale gravity waves are topics of investigation that are in progress by a Ph.D. student, and his work also includes satellite and model data.

In recent work, Correia et al. (2020) used Very Low Frequency (VLF) data to identify small-scale gravity waves over EACF, and compared one case study with all-sky airglow imager data (validation of the technique and methodology for VLF data), showing that the VLF technique can also be used to characterize periodicities and other properties of gravity waves at the base of the ionosphere. This is very interesting and important because the longest gravity waves periodicity (more than 40 min or one hour) can be inferred by VLF as well as short-period gravity waves, and in both cases, the two techniques complement each other since in the summer it is not possible to use the airglow imagers to observe gravity waves because there is not enough darkness to conduct this kind of observation. Also, the optical technique has restrictions of observation during cloudy conditions and full moon periods. On the

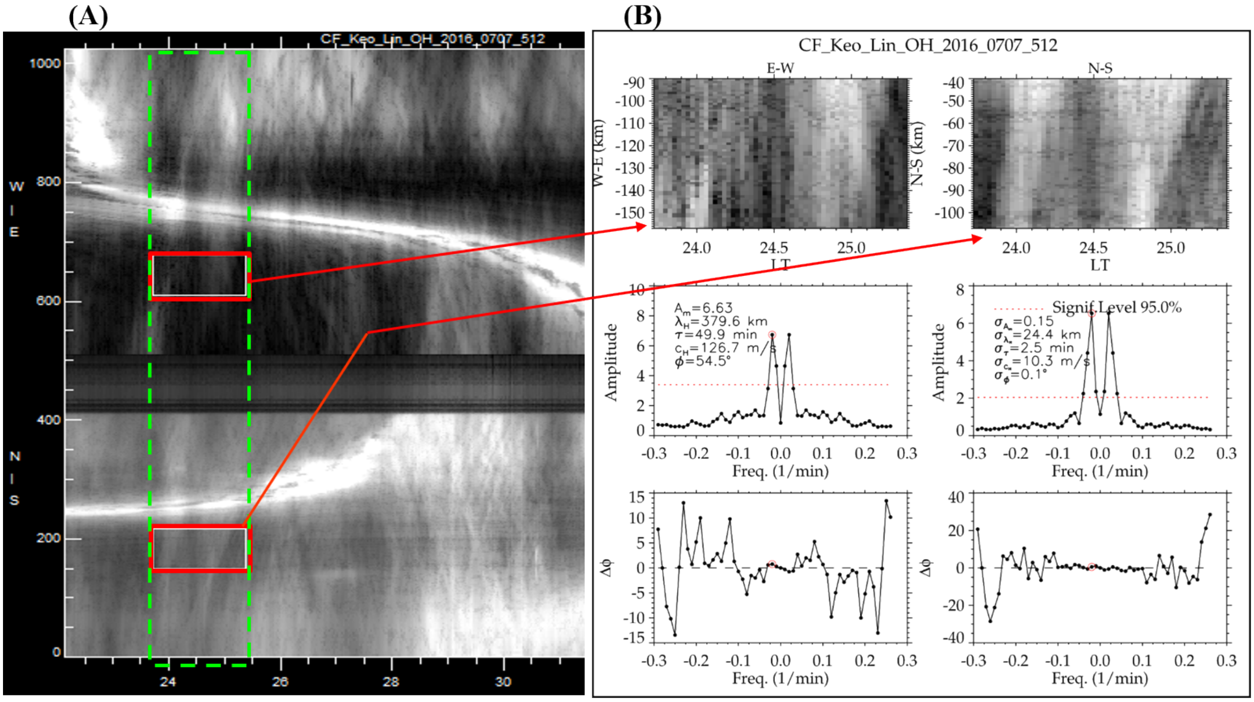

Figure 10. Example of a medium-scale gravity wave observed at EACF on the night of 6-7 of July 2016.

other hand, the images can provide a full view (morphology) of the gravity waves, besides all the observed properties of the wave as well as the exactly azimuthal propagation direction. So, it is important to have distinct views of the same kind of event during the full year. We hope that in a near future, several instruments can provide a complete picture of the dynamics of the upper mesosphere and ionosphere from high to mid-low latitudes, and in this perspective, we also include the meteoric radars that are currently working at EACF and Tierra del Fuego, Southern Argentina, as well as another trail meteor radar that will operate in Santa Maria, RS, Southern Brazil.

SUMMARY

This paper presented a review of the optical techniques used at Comandante Ferraz Antarctic Station (EACF), specifically two photometers, one spectral imager, and two all-sky airglow imagers operated at EACF since 2001 (photometer) up to 2017 (multi-filter all-sky imager). After the rebuilding of the new EACF, the station will be able to return with all kind of instrumentation under PROANTAR/SECIRM projects and through international scientific cooperation. The photometers and spectral CCD imager for temperature measurements shows good data on temperature from 2001 to 2007, as showed in this paper. Intra-seasonal variations in the temperatures were possible to be identified, as well as two maximum and one intense minimum in the winter of 2007, but typically the data shows maximum temperature in the winter and minimum in the summer, noted in the late summer and spring. Atmospheric gravity waves were observed firstly at EACF in a campaign during the winter of 2007, and later on during 2010 and 2011. After that, the observations of gravity waves stopped for two years and restarted in 2014, but only with a few nights of observations due to problems in the power generation nearby the observation site, good data were collected from 2015 to 2017. In 2018, the all-sky imager stopped the operation due to a problem in the instrument because no technicians or researchers were allowed to back to EACF in the years between 2016 and 2018. The gravity wave characteristics, vertical propagation conditions, and some aspects of the wave sources investigations were conducted in the last years by using the airglow images acquired automatically from 2015 to 2017 in the scope of a master thesis finished late in 2020. From that master thesis, one paper was already published (Giongo et al. 2020), and another one is under revision. At the beginning of 2019, the 13 transmitting and receiving antennas of the meteor radar were fixed, and then this system returned its operation in March 2020. In the next summer of 2019/2020, the scientific Antarctic operation was canceled due to the COVID-19 pandemic. Only in the Antarctic Operation of 2021/2022 (specifically in February 2022) was possible to reinstall a new all-sky airglow imager at the Punta Plaza facilities, nearby the EACF, and the noctilucent cloud (NLC) camera was reallocated in the same module (Punta Plaza). Both airglow and NLC cameras captured the first good quality images on the night of February 10, 2022. The radar and cameras are running well until the present moment, and we hope to continue monitoring the upper atmosphere over EACF using ground-based optical and radar techniques along with satellite data. Finally, we need to highlight that airglow images, VLF and meteor radar data can be used to study and characterize gravity waves, planetary waves, and atmospheric tides in the Antarctic Peninsula region and the characterization of these waves can be compared and investigated along with similar data collected at sites of mid-low latitudes in South America (e.g., southern Argentina, and Brazil), giving a general charter of the upper atmosphere dynamics behavior from Antarctic Peninsula to low latitudes in Brazil.

Acknowledgments

E. Correia thanks the Conselho Nacional de Desenvolvimento Científico e Tecnológico (CNPq, processes no: 406690/2013-8 and 303299/2016-9), São Paulo Research Foundation – FAPESP (grant no. 2019/05455-2) for individual research support, and the National Institute for Space Research (INPE/MCTI). C.A.O.B. Figueiredo thank the FAPESP under the processes 2018/09066-8 and 2019/22548-4, and Fundação de Apoio à Pesquisa do Estado da Paraíba (process 303871/2023-7). G.A. Giongo thanks the CNPq for the Ph.D. scholarship grant under the process number 140401/2021-0, and also the Coordenação de Aperfeiçoamento de Pessoal de Nível Superior (CAPES) for the financial support during the master thesis (financial code 001). J.V. Bageston thanks the CNPq for the Junior post-doctorate under process n° 151593/2009-4 and FAPESP for the post-doctorate grant given in 2010 under the process n° 2010/06608-2. . H. Takahashi thanks the CNPq for the senior productive grant number 310927/2020-0. P. Batista thanks the CNPq for the Research Productivity Grant 309140/2020-0. The high-performance all-sky airglow imager installed at EACF in 2014 was provided by the Brazilian Study and Monitoring of Space Weather (Embrace) Program of INPE. We should acknowledge the NSF/OPP grants ATM-0634650 and AGS-1744801 used for the installation, maintenance, and operations of the Drake Antarctic Agile Meteor Radar (DrAAMER) that was deployed at the Brazilian Antarctic Station Comandante Ferraz in 2010, and it was fully repaired during the summer (Feb.-Mar.) of 2020. The authors also acknowledge the support of the Brazilian Ministry of Science, Technology, and Innovation (MCTI) and the Brazilian Space Agency (AEB) who supported the present work under the grants PO 20VB.0009 The Ministry of the Environment (MMA), and Inter-Ministry Commission for Sea Resources (CIRM) for supporting the Antarctic activities.

REFERENCES

BAGESTON JV. 2006. Determinação da temperatura da mesosfera superior utilizando um espectro-imageador. Master Thesis - Brazilian National Institute for Space Research (INPE), São José dos Campos, SP, Brazil, 152p (INPE-14129-TDI/1080). Available online at the following address: http://mtc-m16b.sid.inpe.br/col/sid.inpe.br/MTC-m13@80/2005/11.18.17.25/doc/thisInformationItemHomePage.html (Unpublished).

BAGESTON JV, GOBBI D, TAKAHASHI H & WRASSE CM. 2007. Development of airglow OH temperature imager for mesopheric study. Rev Bras Geof 25: 27-34. https://dx.doi.org/10.1590/s0102-261x2007000600004.

BAGESTON JV, WRASSE CM, BATISTA PP, HIBBINS RE, FRITTS DC, GOBBI D & ANDRIOLI VF. 2011a. Observation of a mesospheric front in a thermal-doppler duct over King George Island, Antarctica. Atmos Chem Phys 11: 12137-12147. https://doi.org/10.5194/acp-11-12137-2011.

BAGESTON JV, WRASSE CM. GOBBI D, TAKAHASHI H & SOUZA PB. 2009. Observation of mesospheric gravity waves at Comandante Ferraz Antarctica Station (62° S). Ann Geophys 27: 2593-2598. https://doi.org/10.5194/angeo-27-2593-2009.

BAGESTON JV, WRASSE CM, HIBBINS RE, BATISTA PP, GOBBI D, TAKAHASHI H, ANDRIOLI VF, FECHINE J & DENARDINI CM. 2011b. Case study of a mesospheric wall event over Ferraz Station, Antarctica (62° S). Ann Geophys 29: 209-219. https://doi.org/10.5194/angeo-29-209-2011.

BAGESTON JV, BATISTA PP, GOBBI D, PAES LEME NP & WRASSE CM. 2012. Mesospheric gravity waves observed at Ferraz Station (62° S) during 2010-2011. INCT-APA Annual Activity Report, p. 26-29. http://dx.doi.org/10.4322/apa.2014.056.

BURITI RA, TSUDA T, FUKAO S, TSUTSUMI M & TAKAHASHI H. 2000. Mesopause temperature observed by airglow OH spectra and meteor echoes at Shigaraki (34.9un, 136.1ue), Japan. Adv Space Res Oxford 26(6): 1005-1008, https://doi.org/10.1016/s0273-1177(00)00047-8.

CORREIA E, RAUNHEITTE LTM, BAGESTON JV & DAMICO DE. 2020. Characterization of gravity waves in the lower ionosphere using very low frequency observations at Comandante Ferraz Brazilian Antarctic Station. Ann Geophys: 38: 385-394. https://doi.org/10.5194/angeo-38-385-2020.

DE LA TORRE A, ALEXANDER P, HIERRO R, LLAMEDO P, ROLLA A, CHMIDT T & WICKERT J. 2012. Large-Amplitude gravity waves above the southern Andes, the Drake Passage, and the Antarctic Peninsula. J Geophys Res Atmos 117: D02106. doi: 10.1029/2011JD016377.

ESSIEN P, PAULINO I, WRASSE CM, CAMPOS JAV, PAULINO AR, MEDEIROS A F, BURITI RA, TAKAHASHI H, AGYEI-YEBOAH E & LINS AN. 2018. Seasonal characteristics of small- and medium-scale gravity waves in the mesosphere and lower thermosphere over the Brazilian equatorial region. Ann Geophys 36: 899-914. https://doi.org/10.5194/angeo-36-899-2018.

FRITTS DC & ALEXANDER MJ. 2003. Gravity wave dynamics and effects in the middle atmosphere. Rev Geophys 41. https://doi.org/10.1029/2001RG000106.

FRITTS, DC, PAUTET P-D, BOSSERT K, TAYLOR MJ, WILLIAMS BP, IIMURA H, YUAN T, MITCHELL NJ & STOBER G. 2014. Quantifying gravity wave momentum fluxes with Mesosphere Temperature Mappers and correlative instrumentation. J Geophys Res Atmos 119(13): 583-13,603. https://doi.org/10.1002/2014jd022150.

FRENCH WJR, KLEKOCIUK AR & MULLIGAN FJ. 2020. Analysis of 24 years of mesopause region oh rotational temperature observations at Davis, Antarctica - part 2: evidence of a quasi-quadrennial oscillation (QQO) in the polar mesosphere. Atmos Chem Phys 20: 8691-8708. https://doi.org/10.5194/acp-20-8691-2020.

GARCIA FJ, TAYLOR MJ & KELLEY MC. 1997. Two-dimensional spectral analysis of mesospheric airglow image data. Appl Optics 36(29): 7374-7385. https://doi.org/10.1364/ao.36.007374.

GIONGO GA ET AL. 2018. Mesospheric front observations by the OH airglow imager carried out at Ferraz Station on King George Island, Antarctic Peninsula, in 2011. Ann Geophys 36: 253-264. https://doi.org/10.5194/angeo-36-253-2018.

GIONGO GA, BAGESTON JV, FIGUEIREDO CAOB, WRASSE CM, KAM H, KIM, YH & SCHUCH NJ. 2020. Gravity wave investigations over Comandante Ferraz Antarctic Station in 2017: general characteristics, wind filtering and case study. Atmosphere 11: 880. https://doi.org/10.3390/atmos11080880.

GOLITSYN GS, SAMENOV AI, SHEFOV NN, FISHKOVA LM, LYSENKO EV & PEROV SP. 1996. Long-term temperature trends in the middle and upper atmosphere. Geophys Res Lett 23(14): 1741-1744. https://doi.org/10.1029/96gl01592.

HINDLEY NP, WRIGHT CJ, SMITH ND & MITCHELL NJ. 2015. The southern stratospheric gravity wave hot spot: individual waves and their momentum fluxes measured by COSMIC GPS-RO. Atmos Chem Phys 15: 7797-7818. https://doi.org/10.5194/acp-15-7797-2015.

HOFFMANN L, GRIMSDELL AW & ALEXANDER MJ. 2016. Stratospheric gravity waves at Southern Hemisphere orographic hotspots: 2003-2014 AIRS/Aqua observations. Atmos Chem Phys 16: 9381-9397. https://doi.org/10.5194/acp-16-9381-2016.

HOZUMI Y, SAITO A, SAKANOI T, YAMAZAKI A, HOSOKAWA, K. 2018. Mesospheric bores at southern midlatitudes observed by ISS-IMAP/VISI: a first report of an undulating wave front. Atmos Chem Phys 18: 16399-16407. https://doi.org/10.5194/acp-18-16399-2018.

JIANG JH, STEPHEN DE, WU DL & WANG DY. 2006. Inter-annual variation of gravity waves in the Arctic and Antarctic winter middle atmosphere. Adv Space Res 38: 2418-2423. https://doi.org/10.1016/j.asr.2005.09.036.

KOGURE M, NAKAMURA T, MURPHY DJ, TAYLOR MJ, ZHAO Y, PAUTET PD, TSUTSUMI M, TOMIKAWA Y, EJIRI MK & NISHIYAMA T. 2023. Characteristics of gravity wave horizontal phase velocity spectra in the mesosphere over the Antarctic stations, Syowa and Davis. J Geophys Res Atmosph 128(6): e2022JD037751. https://doi.org/10.1029/2022JD037751.

LANGHOFF SR, WERNER HJ & ROSMUS P. 1986. Theoretical transition probabilities for the OH Meinel system. J Mol Spectrosc 118(2): 507-529. https://doi.org/10.1016/0022-2852(86)90186-4.

MAEKAWA R. 2000. Observations of gravity waves in the mesopause region by multicolor airglow imaging. Kyoto. Master thesis - Kyoto University, 64 p. (Unpublished).

MEDEIROS AF, TAYLOR MJ, TAKAHASHI H, BATISTA PP & GOBBI D. 2003. An investigation of gravity wave activity in the low latitude upper mesosphere: propagation direction and wind filtering. J Geophys Res 108: 4411. https://doi.org/10.1029/2002JD002593.

MEINEL IAB. 1950. OH emission bands in the spectrum of the night sky. ApJ 111: 555. doi:10.1086/145296.

MEHTA D, GERRARD AJ, EBIHARA Y, WEATHERWAX AT & LANZEROTTI LJ. 2017. Short-period mesospheric gravity waves and their sources at the South Pole, Atmos Chem Phys 17: 911-919. https://doi.org/10.5194/acp-17-911-2017.

NIELSEN K, TAYLOR MJ, STOCKWELL RG & JARVIS MJ. 2006. An unusual mesospheric bore event observed at high latitudes over Antarctica. Geophys Res Lett 33(7). https://doi.org/10.1029/2005GL025649.

PAULINO I, TAKAHASHI H, MEDEIROS AF, WRASSE CM, BURITI RA, SOBRAL JHA & GOBBI D. 2011. Mesospheric gravity waves and ionospheric plasma bubbles observed during the COPEX campaign. J Atmos Sol Terr Phys 73(11-12): 1575-1580. https://doi.org/10.1016/j.jastp.2010.12.004.

PAUTET P-D, TAYLOR MJ, SNIVELY JB & SOLORIO C. 2018. Unexpected Occurrence of mesospheric frontal gravity wave events over South Pole (90°S). J Geophys Res Atmos 123: 160-173. https://doi.org/10.1002/2017jd027046.

PHILLIPS F, BURNS GB, FRENCH WJR, WILLIAMS PFB, KLEKOCIUK AR & LOWE RP. 2004. Determining rotational temperatures from the OH (8-3) band, and a comparison with OH (6-2) rotational temperatures at Davis, Antarctica. Ann Geophys 22(5): 1549-1561. https://doi.org/10.5194/angeo-22-1549-2004.

ROURKE S, MULLIGAN FJ, FRENCH WJR & MURPHY DJ. 2017. A Climatological Study of Short-Period Gravity Waves and Ripples at Davis Station, Antarctica (68°S, 78°E), During the (Austral winter February-October) Period 1999-2013. J Geophys Res Atmos 122: 11388-11404. https://doi.org/10.1002/2017jd026998.

RIND D, SUOZZO R, BALACHANDRAN NK & PRATHER MJ. 1990. Climate change and the middle atmosphere. Part 1: the doubled CO2 climate. J Atmos Sci 47(4): 475-494. doi:10.1175/1520-0469(1990)047<0475:ccatma>2.0.co;2.

ROBLE RG & DICKINSON RE. 1989. How will changes in carbon dioxide and methane modify the mean structure of the mesosphere and thermosphere? Geophys Res Lett 16(12): 1441-1444. https://doi.org/10.1029/gl016i012p01441.

SONG B-G, SONG I-S, CHUN H-Y, LEE C, KAM H, KIM YH, KANG M-J, HINDLEY NP & MITCHELL NJ. 2021. Activities of Small-Scale Gravity Waves in the Upper Mesosphere Observed From Meteor Radar at King Sejong Station, Antarctica (62.22°S, 58.78°W) and Their Potential Sources. J Geophys Res Atmos 126: e2021JD034528. https://doi.org/10.1029/2021JD034528.

TAKAHASHI H, CLEMESHA BR & SAHAI Y. 1974. Nightglow OH (8,3) band intensities and rotational temperature at 23°S. Planet Space Sci 22: 1323-1329. https://doi.org/10.1016/0032-0633(74)90051-8.

WRASSE CM, TAKAHASHI H & GOBBI D. 2004. Comparison of the OH (8-3) and (6-2) band rotational temperature of the mesospheric airglow emissions. Rev Bras Geof 22(3): 223-231. https://doi.org/10.1590/S0102-261X2004000300002.

WRASSE CM. 2000. Observação da temperatura da alta atmosfera através de aeroluminescência. Rev Bras Geof 18(1): 103. https://doi.org/10.1590/s0102-261x2000000100015.

WRASSE C, TAKAHASHI H, MEDEIROS A, LIMA L, TAYLOR M, GOBBI D & FECHINE J. 2007. Determinação dos parâmetros de ondas de gravidade através da análise espectral de imagens de aeroluminescência. Rev Bras Geof 25(3): 257-265. https://doi.org/10.1590/s0102-261x2007000300003.

How to cite

BAGESTON JV, WRASSE CM, GIONGO GA, CORREIA E, FIGUEIREDO CAOB, GOBBI D, TAKAHASHI H, BATISTA PP & COSTA RAB. 2023. Historical line of airglow observations at Comandante Ferraz Brazilian Station: measurements of temperature and studies on gravity waves. An Acad Bras Cienc 95: e20210836. DOI 10.1590/0001-3765202320210836.

Manuscript received on June 14, 2021;
accepted for publication on June 19, 2022

JOSÉ VALENTIN BAGESTON[1]
https://orcid.org/0000-0003-2931-8488

CRISTIANO MAX WRASSE[2]
http://orcid.org/0000-0001-8026-3625

GABRIEL AUGUSTO GIONGO[2]
https://orcid.org/0000-0003-4434-7359

EMÍLIA CORREIA[2,3]
https://orcid.org/0000-0003-4778-3834

COSME ALEXANDRE O.B. FIGUEIREDO[2]
https://orcid.org/0000-0003-4423-5111

DELANO GOBBI[2]
https://orcid.org/0000-0002-8260-1007

HISAO TAKAHASHI[2]
https://orcid.org/0000-0002-8844-8920

PAULO P. BATISTA[2]
https://orcid.org/0000-0002-5448-5803

RICARDO A.B. DA COSTA[4]
https://orcid.org/0000-0002-0027-3565

[1]Instituto Nacional de Pesquisas Espaciais (INPE),
Coordenação Espacial do Sul (COESU), Av. Roraima,
1000, Camobi, 97105-970 Santa Maria, RS, Brazil

[2]Instituto Nacional de Pesquisas Espaciais (INPE), Divisão
de Clima Espacial, Av. dos Astronautas, 1758, Jardim da
Granja, 12227-010 São José dos Campos, SP, Brazil

[3]Universidade Presbiteriana Mackenzie, Centro de Rádio
Astronomia e Astrofísica Mackenzie, Rua da Consolação,
930, Consolação, 01302-907 São Paulo, SP, Brazil

[4]Universidade Federal de Campina Grande (UFCG),
Unidade Acadêmica de Física, Av. Aprígio Veloso, 882,
Bodocongó, 58429-900 Campina Grande, PB, Brazil

Correspondence to: **José Valentin Bageston**
E-mail: jose.bageston@inpe.br

Author contributions

JVB: conceptualization, supervision, original draft preparation, writing-reviewing and editing the final version of the paper. CMW, GAG, EC, COAB, DG, HT, PPB, RABC: reviewing the first and second versions of this paper.